Check for updates

Received: 1 March 2022 | Revised: 27 April 2022 | Accepted: 27 April 2022

DOI: 10.1002/app.52667

RESEARCH ARTICLE

Applied Polymer SCIENCE WILEY

Mechanical and thermal properties of polydimethylsiloxane/magnetite nanocomposites for cancer treatment by localized hyperthermia and photothermal ablation

Chinyerem E. Onyekanne[1] | **Oluwaseun K. Oyewole**[2] | **Ali A. Salifu**[2,3] | **John D. Obayemi**[2,3] | **Vitalis C. Anye**[1] | **Chukwudalu C. Nwazojie**[1] | **Killian C. Onwudiwe**[1] | **Josephine C. Oparah**[1] | **Toyin Aina**[1] | **Chukwudi C. Ezeala**[1] | **Theresa C. Ezenwafor**[1] | **Olushola S. Odusanya**[1,4] | **Winston O. Soboyejo**[1,2,3]

[1]Department of Materials Science and Engineering, Biomaterials Lab, African University of Science and Technology, Galadimawa, Abuja, Nigeria

[2]Department of Mechanical & Materials Engineering, Worcester Polytechnic Institute, Worcester, Massachusetts, USA

[3]Department of Biomedical Engineering, Worcester Polytechnic Institute, Worcester, Massachusetts, USA

[4]Biotechnology and Genetic Engineering Advanced Laboratory, Sheda Science and Technology Complex, Galadimawa Abuja, Nigeria

Correspondence
Winston O. Soboyejo, Department of Mechanical & Materials Engineering, Worcester Polytechnic Institute, 100 Institute Road, Worcester, MA 10609, USA.
Email: wsoboyejo@wpi.edu

Funding information
African Centers of Excellence (ACE), Grant/Award Number: AUST/PAMI/2015 5415-NG; African University of Science and Technology, Grant/Award Number: P126974; the World Bank

Abstract

A combination of experiments and theoretical models is used to study the mechanical and thermal properties of polydimethylsiloxane (PDMS) and magnetite nanoparticle-reinforced PDMS composites with the potential for applications in biomedical implants for localized hyperthermia and photothermal ablation. Composite samples with varying weight fractions (0,1, 5, and 10 wt.%) of Fe_3O_4 nanoparticles were fabricated and tested to determine their stress–strain behavior and fracture toughness. The measured mechanical properties are also compared with predictions from composite and toughening models. The implications of the results are discussed for the design of plasmonic/magnetic nanocomposites with attractive combinations of mechanical and thermal properties that are relevant to laser hyperthermia and photo-thermal-ablation.

KEYWORDS

bioengineering, biomedical applications, morphology, nanocrystals, nanoparticles, nanowires

1 | INTRODUCTION

The design of polymeric matrix composites with attractive combinations of strength and fracture toughness can be achieved by mixing polymer matrices with inorganic reinforcements with complementary properties.[1,2] Thus, in the case of polymeric composites for applications in biomedical implants, there is a need to balance the desired improvements in mechanical or physical properties with the much-needed

 © 2022 Wiley Periodicals LLC.

10974628, 2022, 30, Downloaded from https://onlinelibrary.wiley.com/doi/10.1002/app.52667 by Egyptian National Sci. Network (Enstinet), Wiley Online Library on [06/11/2022]. See the Terms and Conditions (https://onlinelibrary.wiley.com/terms-and-conditions) on Wiley Online Library for rules of use; OA articles are governed by the applicable Creative Commons License

biocompatibility that is needed for effective applications in the human body.[3–5]

PDMS is an example of a biocompatible polymer matrix that has received considerable attention due to its excellent combination of biocompatibility, optical transparency, mechanical and thermal properties.[6]

Polydimethylsiloxane (PDMS) is a silicon-based organic polymer composed of a repeating unit [SiO(CH3)].[7] It is an elastomer polymer that is often processed at the micrometer scale for many scientific and engineering applications.[7] PDMS is also easy to process, nontoxic, and nonflammable. It also exhibits attractive combinations of elastic/viscoelastic properties, optical transparency[8] and, biocompatibility, high gas permeability, high compressibility, chemically inertia, high flexibility; and chemical/thermal stability.[9,10]

PDMS can also be mixed with different reinforcements to produce composites with engineered combinations of mechanical, magnetic, plasmonic, and thermal properties.[10–12] Such combinations of properties, along with the biocompatibility of the PDMS matrix, make PDMS composites attractive for applications in biomedical devices.[6,9,13]

On the other hand, MNPs have received significant attention because of their attractive combinations of physico-chemical and magnetic properties, and the ease with which they form composite mixtures with organic or inorganic compounds. Thus, MNP-reinforced composites have been developed recently for biomedical applications.[14] Within this context, magnetite nanoparticles have attracted widespread attention due to their biocompatibility,[14–17] low cost,[14] chemically stability, and unique magnetic properties.[14,15] In addition, magnetite nanoparticles are chemically inert materials with low toxicity levels.[16] They are also characterized by their superparamagnetic behavior, and their immune induction capacity, making potential systems for antigen delivery.

Among the magnetic particles with dual functions of magnetism and NIR absorption, magnetite nanoparticles stand out as nanoparticles for photothermal therapy. IONs have great potential for biomedical applications, due to their biocompatibility, biodegradability and easy functionalization for specific applications[15,18,19] These properties, and the widespread acceptance of lack of toxicity, make magnetite a good candidate to be used in cancer therapeutics via drug delivery, magnetic hyperthermia, photodynamic, and photothermal applications.[15]

However, despite these characteristics, there are also some drawbacks associated to it such as; aggregation and instability due to the rapid biodegradation of bare MNPs in biological media, which continue to hinder the transition to clinical applications, In order to overcome these challenges, nanocomposites (NCs) consisting of polymers and MNPs have been proposed for the localized treatment of tumor tissue via localized hyperthermia.[20,21] These materials offer new opportunities for the development of novel cancer treatment modalities. They have also been combined with materials for the controlled release of therapeutic drugs to synergistically treat cancer by the combined effects of localized drug release and heat. These materials offer unique mechanical, electrical, optical, and thermal properties.

Researchers have shown that incorporation of nanoparticle fillers enhances the mechanical properties of PDMs. Incorporating carbon nanotube enhances the elastic modulus and reduces the hardness of PDMS.[22] The nanoparticle-PDMS films have a higher Young's modulus than pure PDMS films and also show enhanced antibacterial properties when reinforced with silver, gold, silica, and platinum.[23,24] Increase in Young's modulus; decrease in tensile strength; decrease in hardness with increasing nanoparticle concentration were observed when magnetite nanoparticles were incorporated in PDMs.[25] Incorporation of TiO_2 (titanium dioxide) nanoparticles exhibits lower surface roughness, higher contact angle values, and better corrosion protection performance.[26]

One such application is in PDMS/magnetite nanoparticle composite devices that are being developed for the thermal treatment of cancer by laser/magnetite interactions that can give rise to programmed cell death (hyperthermia) or photo-ablation, which depend on the induced temperature profiles. In such scenarios, the plasmonic interactions can give rise to localized hyperthermia, when the induced temperatures are between 41 and 44°C, while even higher temperatures can give rise to necrosis and photoablation.[27]

There is, therefore, need to the potential to engineer novel nanocomposites that can be implanted into prior tumor regions, following tumor resection by surgery. In such cases, the localized heating associated with laser/magnetic nanoparticle interactions can be used to "kill" or "ablate" residual tumors, following the resection of tumors.[28]

Considering the biocompatibility of both the matrix and the reinforecement that are being explored for the treatment. Polydimethylsiloxane, has been widely used in the biomedical industry. Although, elastomers (rubbers) have been the object of study of many researchers due to some of their interesting biomechanical characteristics, such as: flexibility, chemical stability, and resistance to corrosion. Among these elastomers in the market, PDMS stands out in recent years, because of its biocompatibility and its biomechanical behavior is similar to biological tissues.[6] It is biocompatible and biostable and has the least impact on the tissue.[29] It does not cause inflammatory response due to the reaction of the immune system thus damaging the functioning of the implanted device.[30]

10974628, 2022, 30, Downloaded from https://onlinelibrary.wiley.com/doi/10.1002/app.52667 by Egyptian National Sci. Network (Enstinet), Wiley Online Library on [06/11/2022]. See the Terms and Conditions (https://onlinelibrary.wiley.com/terms-and-conditions) on Wiley Online Library for rules of use; OA articles are governed by the applicable Creative Commons License

PDMS is one of the most successful polymers, because when implanted it only causes a brief inflammatory reaction in the organism, which explains its widespread use in personal care and topical skin applications.[31] It has also been reported that iron oxide nanoparticles are more widely used than other magnetic nanoparticles due to their biocompatibility and chemical inertness that make them suitable for medical, pharmaceutical and therapeutic applications.[16,32,33] Also magnetite/PDMS nanocomposites are biocompatible, inert and nontoxic,[34] making them excellent candidates for applications in biomedical devices for breast cancer treatment.

Nanoparticle concentration on the mechanical properties of PDMS under different preparation conditions.[10,35–37] Their results showed, among others, that there were significant differences in Young's moduli for the range of curing temperatures tested.

Recently, polymer nanocomposites reinforced with low fraction of filler particles have attracted growing interest due to their fascinating properties. The incorporation of nano fillers with high aspect ratio and extremely large surface area into polymer has seen to improve their mechanical performances significantly. Kwon et al.[38] investigated the enhanced mechanical properties of polymer nanocomposites using dopamine-modified polymers at nanoparticle surfaces in very low molecular weight polymers. They reported a dramatic enhancement of the mechanical properties of polymer nanocomposites (PNCs). Their results showed that attractive interactions between particles induced by DOPA-mPEG grafting dramatically improve the mechanical properties. PNC consists of poly (ethylene glycol) (PEG) and silica nanoparticles whose surfaces are modified with dopamine modified PEG (DOPA-mPEG) brush polymers.

In a review by Amit Kumar et al.[39] on the mechanical properties of polymer composites reinforced by carbon nanotubes and grapheme, CNTs have reported to have excellent mechanical and thermal properties. Recently, Konku-Asase et al.[25] studied the effects of standard curing temperature conditions on bulk mechanical properties of PDMS nanocomposites the result also showed an increase for Young's modulus (E) and a decrease of the ultimate tensile strength (UTS) of with increasing concentration of the NPs and also hardness was seen to increase with curing temperature but decreased with concentration. To the best of our knowledge, there has been no reported investigation of the mechanical properties of the nanocomposites for hyperthermia treatment and in comparison with the mechanical properties of the breast tissue.

However, the implants must also have controlled mechanical properties for them to be compatible with the surrounding tissues. Thus, to avoid stress shielding effects, the implants can be engineered to have comparable moduli to those of the surrounding matrix materials. Similarly, the implants must also be resistant to failure by deformation and cracking phenomena, which can be engineered by the control of composite strength and fracture toughness.[40]

There is, therefore, a need to develop novel composites that can be implanted into prior tumor regions to enable the thermal treatment of residual tumors via controlled hyperthermia or photoablation. This will be explored in the current study using model PDMS/magnetite nanoparticle composites.

This article will use a combination of theory and experiments to study the effects of magnetite nanoparticle volume fraction on the thermal properties (thermo-gravimetric analysis (TGA), differential scanning calorimetry, (DSC), and Fourier-transform infrared (FTIR) and mechanical properties (stress–strain behavior and fracture toughness) of composites that are relevant to potential applications in the treatment of triple-negative breast cancer. The implications of the results will also be discussed for the development of future implantable biomedical devices for localized hyperthermia and/or laser photoablation.

2 | THEORY

2.1 | Models for the prediction of composite mechanical properties

Mechanical property data obtained from experiments can be used in composite models for the prediction of mechanical properties. The simple rule-of-mixture models give:

$$E_c = E_p V_p + E_m V_m \tag{1}$$

and

$$\sigma_c = \sigma_p V_p + \sigma_m V_m, \tag{2}$$

where E_c is the composite Young's modulus, E_p and E_m are the nanoparticles and matrix young modulus, σ_m and σ_p are tensile strength of matrix and nanoparticles, and V_m and V_p are the volume fractions of both the matrix and nanoparticles.

In the case of particle-filled composites, Guth and Smallwood[41] have developed the following expression for the Young's moduli of particle-filled composites. This is given by:

$$E_c = E_m\left(1 + 2.5\phi_f + 14.1\phi_f^2\right), \tag{3}$$

where E is Young's modulus and ϕ_f is the volume fraction of particles. Subscripts m, f, and c denote matrix, filler, and composite, respectively.

10974628, 2022, 30, Downloaded from https://onlinelibrary.wiley.com/doi/10.1002/app.52667 by Egyptian National Sci. Network (Enstinet), Wiley Online Library on [06/11/2022]. See the Terms and Conditions (https://onlinelibrary.wiley.com/terms-and-conditions) on Wiley Online Library for rules of use; OA articles are governed by the applicable Creative Commons License

A modification to Equation (3) is presented in the Shear lag model[42] which can be used to estimate the modulus of composite materials. This is given by:

$$E_c = E_m V_m (1 - V_p) + V_p E_p \left(\frac{1 - tanh(x)}{x} \right), \quad (4)$$

where

$$x = \frac{l}{d} \left[(1 + \upsilon_m) \left(\frac{E_p}{E_m} \right) Ln(V_p)^{-1/2} \right]^{-1/2} \quad (5)$$

and E_c, E_m, and E_p are the respective Young's moduli of the composite, matrix, and filler particles; V_m and V_p are the respective volume fractions of matrix and filler particles; $\frac{l}{d}$ is the aspect ratio, and υ_m is Poisson's ratio of the matrix.

The shear lag model was first developed by Cox[43] and later modified by Nardone and Prewo.[44] The model applies to composites reinforced with whiskers or short fibers. The model assumes that the applied load is transferred from the matrix to the nanoparticle via shear.

The semiempirical equations suggested by Halpin–Tsai are another way of predicting the composite properties.[45,46] Halpin–Tsai model demonstrates the effect of reinforcement on the of composite as a function of filler aspect ratio and volume fraction. The elastic modulus of composite material in Halpin–Tsai model[45,46]:

$$\frac{E_c}{E_m} = \frac{(1 + \zeta \eta V_f)}{(1 - \zeta \eta V_f)}, \quad (6)$$

$$\eta = \frac{\left(\frac{E_f}{E_m} - 1 \right)}{\left(\frac{E_f}{E_m} + \zeta \right)}, \quad (7)$$

where ζ is a shape factor and V_f is the volume fraction of the particle. They have shown that ζ must lie between zero and infinity. The value of ζ must also correlate with the geometry of the reinforcing phase especially with the aspect ratio (w/t) of the particle, where w is the length of the particle and t is the thickness. Generally, the shape factor for particulate composites has been predicted to have a value of 2 for spherical particles, while the aspect ratio is unity.[46,47]

Finally, the strength of composite material has also been modeled by Arsenault and Taya.[42,48] This is given by:

$$\sigma_{yc} = \sigma_m 0.5 V_p \left(2 + \frac{l}{d} \right) + \sigma_m (1 - V_p), \quad (8)$$

where σ_{yc} and σ_m are the respective yield strengths of the composite and matrix.

2.2 | Fracture toughness

The stress intensity factor, K, at the tip of the crack in a single edge notched specimen under tension is given by[49]:

$$K = \frac{P}{(BB_N W)^{0.5}} f\left(\frac{a}{W} \right), \quad (9)$$

where $f(a/W)$ is a geometry function that depends only on a/W and is independent of the thickness. P is the applied force, B is the specimen thickness before side-grooving and B_N is the net section thickness after side-grooving. In this study, no side-grooving was introduced in the fabrication of the initial crack. Thus, B is the same as B_N. The well-known stress intensity factor handbook of Tada et al.[50] has the K solution for SENT specimens with shallow to deep cracks in pure tension, and the geometry function is expressed as the following polynomial function:

$$f_1\left(\frac{a}{W} \right) = 1.122 - 0.231 \left(\frac{a}{W} \right) + 10.55 \left(\frac{a}{W} \right)^2 - 21.71 \left(\frac{a}{W} \right)^3 + 30.382 \left(\frac{a}{W} \right)^4, \quad (10)$$

where a is the crack length and W is the width. The solution is valid for $a/W \leq 0.6$ and accurate within 0.5%.[50]

2.3 | Crack bridging model

Crack bridging by uncracked ligaments is one of the possible toughening mechanisms that can occur in particle-reinforced nanocomposites. Thus, it is the uncracked ligaments, and not the individual particles, that are responsible for the crack-tip shielding. This results in the shielding of the crack-tip by the ligaments that are left behind along the bridge lengths, L, behind the crack-tip.

Small scale bridging corresponds to bridging lengths that are less than 0.5 mm[51] while large scale bridging typically corresponds to bridging lengths that are greater than 0.5 mm. In the small-scale bridging regime, an idealized elastic–plastic spring model, proposed originally by Budiansky et al.,[52] crack bridging can be simulated using a series of distributed springs that are connected to crack faces.

Under small-scale bridging conditions (the length of the bridging zone is very small compared to specimen dimensions).[53] For SSB conditions, the toughening due to crack bridging is given by[51]:

10974628, 2022, 30, Downloaded from https://onlinelibrary.wiley.com/doi/10.1002/app.52667 by Egyptian National Sci. Network (Enstinet), Wiley Online Library on [06/11/2022]. See the Terms and Conditions (https://onlinelibrary.wiley.com/terms-and-conditions) on Wiley Online Library for rules of use; OA articles are governed by the applicable Creative Commons License

$$\Delta K_{SSB} = \sqrt{\frac{2}{\pi}\alpha V_f \int_0^L \frac{\sigma_Y}{\sqrt{X}} dx}, \quad (11)$$

where ΔK_{SSB} is toughening due to SSB, a is the constraint/triaxiality factor, V_f is the volume fraction of the nanoparticle, L is the length of the bridging ligament, σ_y are the uniaxial yield stress and x corresponds to the distance from the crack tip.

If the initiation fracture toughness, K_i, is determined from experiments using stress intensity equations for SENT specimens, then the composite fracture toughness, K_R, can be obtained from the following expression:

$$K_R = K_i + \Delta K_B, \quad (12)$$

where ΔK_B represents toughening contribution for SSB conditions.

2.4 | Crack deflection model

Another possible toughening mechanism is shielding by crack deflection. This occurs when the crack paths are perturbed by reinforcements that cause the crack to deflect by tilting and/or twisting[53] resulting in nonplanar crack propagation. The toughening mechanism for different inclusions was analyzed by Faber and Evans (1983) who proposed the following expression for titling and twisting around spherical inclusions[53]:

$$\frac{K_c}{K_o} = \left(\frac{E_c}{E_o}(1 + 0.87f)\right)^{1/2}, \quad (13)$$

where E_c is the Young's modulus of the modified matrix, and E_o is the Young's modulus of the unmodified matrix. As indicated in Bengisu and Inal,[54] two conditions can lead to crack deflection: residual strain in the composite and weak matrix/second-phase interfaces. Residual strain can be generated by elastic modulus and/or thermal expansion mismatch between the matrix and second-phase anisotropy of thermal expansion in a monolithic or composite material.

3 | MATERIALS AND METHODS

3.1 | Materials

Sylgard 184 silicone elastomer kit was purchased from Dow Corning Corporation (Auburn, MI, USA) while Iron oxide Nanopowder (Fe_3O_4) (high purity, 99.5%, 15–20 mm) was purchased from US Research Nanomaterials, Inc. (Houston, TX, USA). These materials were used as received for the fabrication of nanocomposite samples.

3.2 | Fabrication of nanocomposites

Magnetite nanoparticles with average diameter sizes of 15–20 nm were mixed with PDMS to obtain nanocomposites with weight percentages of 1, 5, and 10 wt.%. Initially, the base kit of the PDMS elastomer was mixed with the curing agent at a weight ratio of 10:1. The mixture was then stirred vigorously until a completely uniform and cross-linked system was formed. Thereafter, powdered MNPs were added to the uniform cross-linked PDMS.

The resulting mixtures were then poured into molds before degassing at room - temperature (~25°C) to remove all the trapped air bubbles. This was done for 30 min at a pressure of 25 mmHg in a vacuum oven. Finally, the cast MNP-PDMS mixtures were cured for 4 h at a temperature of 60°C.

3.3 | Microstructure and physico-chemical characterization

Fourier transform infrared (FTIR) spectroscopy (IRSpirit Model, Shimadzu, Kyoto, Japan) was used to determine the absorbance of the PDMS/magnetite nanoparticle composites, while the surface morphologies of the PDMS and PDMS/magnetite nanocomposites were characterized using scanning electron microscopy, SEM (back-scattered and secondary imaging) (JEOL 7000F, JEOL Inc., Peabody, MA USA).

The thermal stability of the nanocomposites was also investigated by TGA (TG 209 F1 Libra, NETZSCH, Selb, Germany) and differential scanning Calorimetry (DSC). (DSC 214 Polyma, NETZSCH, Selb, Germany) This was done to evaluate the effect of the nanoparticles with the polymer matrix. TGA thermograms were obtained between 25 and 800°C with a constant heating rate of 20 K/min under nitrogen gas. This was done using alumina crucibles containing 10 mg of sample. This was used to identify the decomposition temperatures, the glass transition temperatures (T_g), and the melting temperatures (T_m), respectively.

For the DSC analysis, 10 mg of the nanocomposites of different volume fractions were weighed, respectively. In each case, samples were sealed in aluminum pans. The samples were then heated in an inert nitrogen atmosphere with a nitrogen flow rate of 20 ml/min that was

10974628, 2022, 30, Downloaded from https://onlinelibrary.wiley.com/doi/10.1002/app.52667 by Egyptian National Sci. Network (Enstinet), Wiley Online Library on [06/11/2022]. See the Terms and Conditions (https://onlinelibrary.wiley.com/terms-and-conditions) on Wiley Online Library for rules of use; OA articles are governed by the applicable Creative Commons License

subjected to a heating cycle between 20 and 250°C with an empty reference aluminum pan. The data obtained were then analyzed by NETZSCH Proteus-7.0 software (NETZSCH, Selb, Germany).

3.4 | Mechanical testing

Mechanical tensile testing was carried out in an Instron electro-mechanical testing machine (Instron Model 68SC-1, Norwood, MA, USA). The dog-bone samples were cast in an acrylic mold with a length of 57.5 mm, a width of 9.5 mm, and a thickness of 3 mm. The samples were cast following ASTM D638 type 1 V code specification. The bottom clamp was attached to a 50 N load cell while the upper clamp was attached to the crosshead in the Instron machine.

The Instron machine was operated at the speed of 1×10^{-4} mm/s using Bluehill Universal software. Every specimen was positioned to be vertically well-aligned between the clamps. All tests were run until the entire cross-section has fractured. During the tensile testing process, a camera was placed close to the crack regime on the side to monitor the true displacement in the samples. The collected video was then analyzed using Image J software package (NIH, Bethesda, MD) to extract the strains.

3.5 | Fracture toughness

Mode I fracture toughness (K_{IC}) tests were carried out on PDMS and PDMS/magnetite nanocomposite specimens with weight percentages of magnetite nanoparticles of 1, 5, and 10%. The specimens were tested in the same Instron testing machine that was used for the tensile tests. The tests were performed on single edge notched tension (SENT) fracture mechanics specimens with a notch to width ratio, *a/W*, of 0.45. The specimens were subjected to monotonic loading at a crosshead speed of 0.004 mm/s.

Four replicate specimens were tested for each blend composition. The notch was created by drawing a razor blade across the notch tip before testing. All the specimens failed by unstable crack growth, and hence only a single initiation value of the fracture toughness was obtained from each specimen. The maximum load, *P*, obtained from the load–displacement curves were used to determine the fracture toughness using Equation (9).

Resistance-curve experiments were used to study the crack/microstructure interactions and toughening mechanisms associated with crack growth. The R-curve experiments were carried out using the same specimen geometry that was used to study of fracture toughness. Crack growth was monitored using the proscope with video monitoring using an optical microscope and scanning electron microscope. The crack growth was observed and analyzed using the Image J software package (NIH, Bethesda, MD, USA), while the stress intensity factors were obtained from Equation (9).

4 | RESULTS AND DISCUSSION

4.1 | Microstructure

To gain insight into the distributions of the nanoparticles, a scanning electron microscope (SEM) was used to observe the magnetite nanocomposite. Figure 1a–d shows micrographs of the magnetite nanocomposites with different weight fractions of MNP particles. The results show the heterogeneous distribution of nanoparticles within the matrix. A similar distribution of the nanoparticles was also observed in the SEM images using back-scattered SEM imaging (Figure S1). Magnetite nanoparticles are observed within the PDMS matrix.

The microstructures of the three nanocomposites show inhomogeneous distributions of nanoparticles (Figure 1b–d). In the case of the nanocomposites with reinforcement weight fractions of 10%, some particle agglomeration was observed, as shown in Figure 1d. Some evidence of microcracking was also observed in the PDMS matrix, with the incidence of microcracking increasing with increasing weight fraction of magnetite nanoparticles. These results from SEM showed that the nanoparticles were not well-dispersed throughout the polymer matrix.

4.2 | FTIR analysis

The FTIR spectra obtained for the plain PDMS and PDMS-MNP nanocomposites are presented in Figure 2a. The spectra exhibited peaks at 787 cm^{-1} associated with —CH_3 rocking and Si—C stretching in Si—CH_3 and at 1010 cm^{-1} due to Si—O—Si stretching. There were also peaks at 1275 and 2962 cm^{-1} corresponding to CH_3 deformation in Si—CH_3 and asymmetric CH_3 stretching in Si—CH_3, respectively,[55] while magnetite's nanoparticle signature corresponds to 668 to 526 cm^{-1} peaks.[56,57] The results show that these bands were well maintained for the PDMS samples, irrespective of the weight percentage of MNPs. Thus, no primary chemical bonds were formed during the fabrication process and the PDMS-MNP nanocomposites were simply pure mixtures of PDMS and magnetite nanoparticles.

10974628, 2022, 30, Downloaded from https://onlinelibrary.wiley.com/doi/10.1002/app.52667 by Egyptian National Sci. Network (Enstinet), Wiley Online Library on [06/11/2022]. See the Terms and Conditions (https://onlinelibrary.wiley.com/terms-and-conditions) on Wiley Online Library for rules of use; OA articles are governed by the applicable Creative Commons License

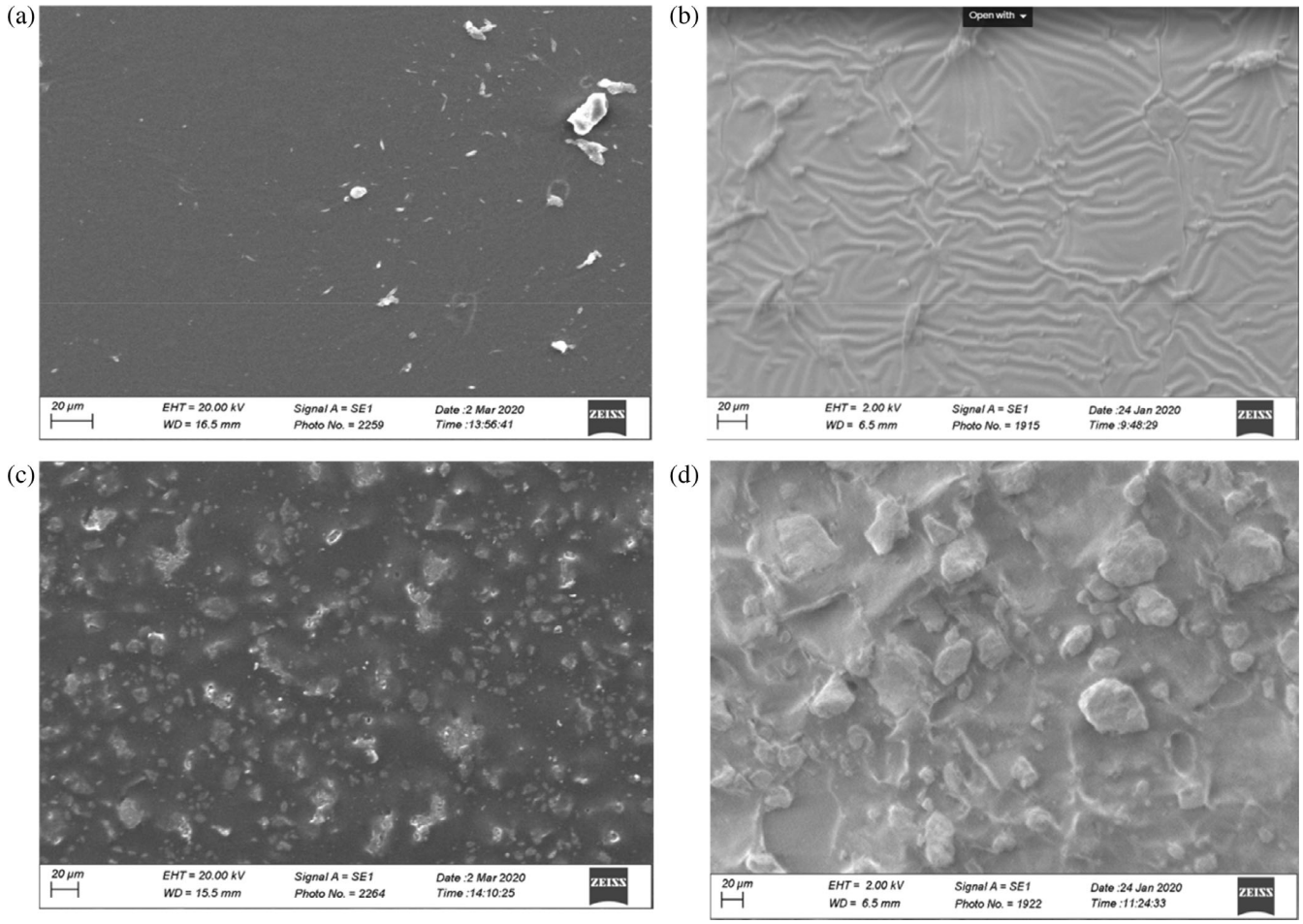


FIGURE 1 SEM images of the composite for (a) pure PDMS, (b) PDMS + 1% MNPs, (c) PDMS + 5% MNPs, and (d) PDMS + 10% MNPs

4.3 | Thermal properties

The effects of magnetite nanoparticles on the thermal stability of the PDMS-based composites, with different volume fractions of nanoparticles, were investigated by TGA. The typical TGA weight loss values for pure PDMS and PDMS nanocomposites, at different ranges of heating temperatures between 25 and 800°C under nitrogen, are presented in Figure 2b. The result shows that all TGA curves reveal degradation in a single step. There is a slight change in the presence of nanoparticles compared to the pure PDMS.

When the operating temperature is below 200°C, they can be stably operated without thermal decomposition. The presence of Magnetite nanoparticles could hinder the movement of volatiles to enhance the thermal stability of PDMS composites.[58] Regardless of the presence of MNPs, the trend of thermal degradation is synchronous as the temperature increases. Weight loss until 400°C is mainly related to loss of water and physical adsorbed layer.[58]

Above 400°C, it can be observed that the temperatures of initial decomposition for the nanocomposites shifts to higher values compared with pure PDMS, which indicates the presence of magnetite as a filler enhances the thermal stability of the PDMS matrix in PDMS nanocomposites. According to several authors[58–60] this degradation is due to the phenomenon of depolymerization around 400–600°C.

This means that the addition of magnetite nanocomposites increases the depolymerization temperature. This is as a result of the presence of an inorganic sample that sustains even at higher temperatures. It was also observed that agglomeration plays a role in the 10 wt.% composite, compared to the 1 and 5 wt.% composites.[61] Overall, the incorporation of nanofillers provided higher thermal stability of the nanocomposites than that of PDMS. This is attributed to the thermal stability of the MNP fillers, as described in prior work.[62,63]

DSC technique was also used to investigate the response of polymers to heating. It has been widely applied in the investigation of numerous phenomena

10974628, 2022, 30, Downloaded from https://onlinelibrary.wiley.com/doi/10.1002/app.52667 by Egyptian National Sci. Network (Enstinet), Wiley Online Library on [06/11/2022]. See the Terms and Conditions (https://onlinelibrary.wiley.com/terms-and-conditions) on Wiley Online Library for rules of use; OA articles are governed by the applicable Creative Commons License

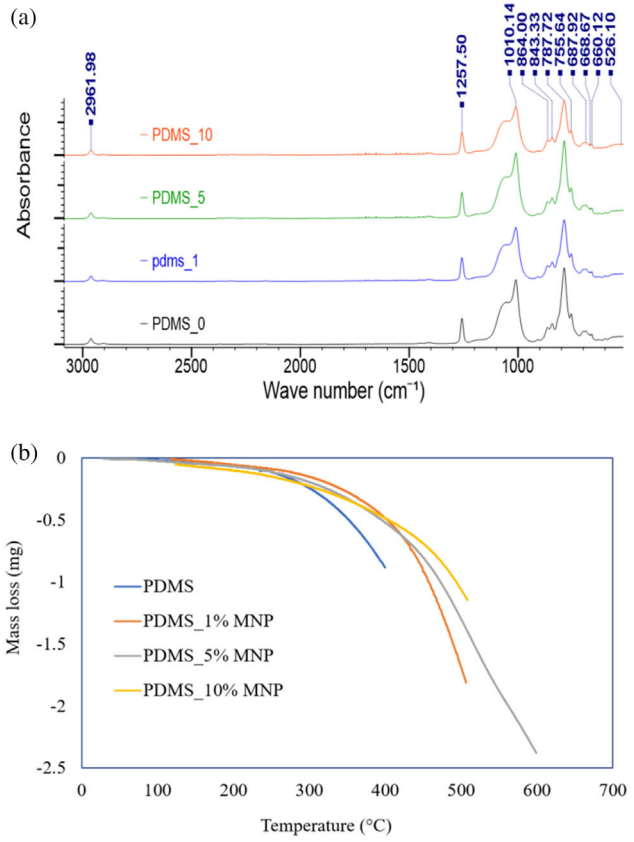


FIGURE 2 (a) FTIR spectroscopy of the matrix and nanocomposites and (b) TGA thermograms of the nanocomposites and the matrix [Color figure can be viewed at wileyonlinelibrary.com]

occurring during thermal heating of polymer nanocomposites involving glass transition (T_g), melting (T_m), crystallization, and curing temperatures. The technique was used to highlight appreciable enhancement in T_g brought about by the presence of the nanoparticles. The experiment was performed using NETZSCH TG 209F1. The samples were heated from 0 to 300°C with a heating rate of 10.0 (K/min).

A representative DSC thermogram is shown in Figure S2. The results show that inflection point increases with increase in volume fraction (PDMS = 44.4; 1% = 56.3; 5% = 89.5, and 10% = 178.2°C) as seen in Table 1. No clear trend was observed in the exothermic peak with increasing magnetite nanoparticle volume fraction.

Therefore, the thermomechanical analysis shows that the overall incorporation of nanofillers provides higher thermal stability of the nanocomposite for neat PDMs, due to the high heats resistance and thermal stability of the MNP fillers as reported in previous studies.[62,63] The glass transition temperature was seen to be affected by the addition of the nanoparticles.[58]

TABLE 1 DSC analysis of PDMS nanocomposites

Glass transition (°C)	0%	1%	5%	10%
Onset	87.3	55.7	129.7	167.1
Mid	121.0	108.8	145.8	200.2
Inflection	44.4	56.3	89.3	178.2
End	154.4	61.5	161.8	227.0
Complex peak				
Peak	79.9	217.1	151.9	215.2
Onset	44.5	56.6	89.3	167.1
End	247.2	242.8	218.2	241.1

4.4 | Mechanical properties

4.4.1 | Strength and Young's moduli

The strength of a material is defined as the maximum stress that the material can sustain under uniaxial tensile loading. For micro-and nano-particulate composites, this relies on the effectiveness of stress transfer between matrix and fillers. For poorly bonded particles, the stress transfer at the particle/polymer interface is inefficient. As in fiber-reinforced composites, the quality of adhesion at the interface is of crucial importance for the behavior of the composite reinforced with nanoparticles.

The adhesion at the interface determines the load transfer between the components. The Young's modulus, however, is not affected by this parameter because of small loads or displacements. However, for composites containing well-bonded particles, the addition of particles to a polymer will lead to an increase in strength especially for nanoparticles with a high surface.[64]

The influence of reinforcement volume fraction on the elastic modulus and tensile strength of the polymer matrix reinforced with different volume fractions of magnetite has been investigated. The strengths and the moduli obtained from the experiment are summarized in Table 2. This shows the average values and their standard deviations obtained from a minimum of four repetitions. The results show that the strength increases by 40%, as more weight fraction of nanoparticles increases between 0%–5%. However, in the case of the composite with 10 vol.% of magnetite, the strength reduces.

The stress–strain curves of the matrix and the composites are presented in Figure 3a. The stress–strain curves show considerable nonlinearity before reaching the breaking stress, that is, they show apparently-brittle structure. Each curve shows maximum stress, which is assumed to be the ultimate tensile strength of the material. The stress–strain rate is highest at 5% and reduces at 10%, as also seen in Table 2 and Figure 3a. The strength

10974628, 2022, 30, Downloaded from https://onlinelibrary.wiley.com/doi/10.1002/app.52667 by Egyptian National Sci. Network (Enstinet), Wiley Online Library on [06/11/2022]. See the Terms and Conditions (https://onlinelibrary.wiley.com/terms-and-conditions) on Wiley Online Library for rules of use; OA articles are governed by the applicable Creative Commons License

TABLE 2 The mechanical properties of the PDMS nanocomposite

Sample	Young modulus (MPa)	Tensile strength (MPa)	Fracture toughness (MPa $m^{0.5}$)
PDMS	1.873 ± 0.01	0.657 ± 0.23	0.0241 ± 0.05
1%	2.043 ± 0.10	0.696 ± 0.21	0.0263 ± 0.06
5%	2.234 ± 0.14	1.000 ± 0.24	0.0319 ± 0.015
10%	2.544 ± 0.05	0.481 ± 0.27	0.0345 ± 0.01

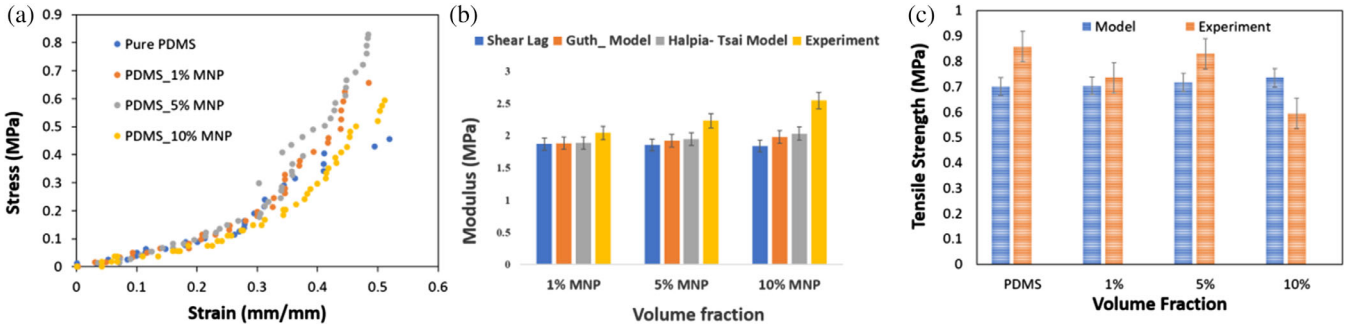


FIGURE 3 (a) Plot of stress versus strain curve, (b) plot of Young's modulus versus volume fraction of the nanocomposites comparison model plot, and (c) strengthening mechanism model plot [Color figure can be viewed at wileyonlinelibrary.com]

decrease at 10% may be as a result of nanoparticle agglomeration at a higher volume percentage, the agglomeration of the nanoparticles results in stress concentrations in regions in which particle touching is associated with inhomogeneous distributions of reinforcements. This explains the reduction in composite strength as the particle weight fraction increases between 5% and 10% weight fraction. It was also observed that the graph is divided into two regions.

At first, for strains <0.3 mm, the strains in the matrix and the composites follow the same trend, and are almost the same at low strain rates, while in the second regime, strains ≥0.3 mm, very high stresses were observed at high strain rates.

The results show that the matrix has a low tensile strength, compared to the composites reinforced with nanoparticles in which the highest strengths were observed in the case of nanocomposites reinforced with 5% of magnetite nanoparticles. The improvements in composite strength are attributed to the effects of deformation restraint by the magnetite nanoparticles. However, for composites reinforced with more than 5 wt.% of magnetite, the trends in the strengths are attributed to the effects of particle agglomeration.[65]

The Young's modulus increases almost linearly from 1.873 ± 0.01 MPa (for pure PDMS) to 2.544 ± 0.05 MPa (for the composite reinforced with 10 wt.% (Table 2). The observed increase of approximately 24% is in agreement with previously reported values for PDMS-based nanoparticle reinforced composite materials.[54,55,61,62] The variations in results are also dependent on processing conditions[54,55] and the molecular weight of the matrix PDMS.[61,62]

4.4.2 | Strengthening mechanisms

The understanding of the strengthening mechanisms of the nanocomposite is important for robustness and improved performance. The mechanical properties of composites reinforced with particles are controlled by a complex interaction between the matrix and the reinforcement, such as interfacial bonding strength, deformation compatibility when the load is applied and thermal expansion mismatch due to the different expansion coefficients. Some other factors can be considered to determine the failure of the composites, such as pore density, interfacial debonding of nanoparticle/polymer nanocomposite, and the distribution of MNP particles.

The weight fraction of magnetite nanoparticles and the elastic properties of the matrix were first converted to volume fraction using rule of mixture as seen in Table 3 and incorporated into empirical strengthening models described in Section 2. The dispersion strengthening consists of three main contributions, replacing a portion of low Young's modulus polymer with more rigid particles which are size-dependent, chain stiffening due to dynamical and packing restriction at the segment scale which is also related to the particle size and finally, stress transfer between the matrix and the particle due to shear stress

10974628, 2022, 30, Downloaded from https://onlinelibrary.wiley.com/doi/10.1002/app.52667 by Egyptian National Sci. Network (Enstinet), Wiley Online Library on [06/11/2022]. See the Terms and Conditions (https://onlinelibrary.wiley.com/terms-and-conditions) on Wiley Online Library for rules of use; OA articles are governed by the applicable Creative Commons License

developed at the particle-matrix interface.[66] The reinforcing particles tend to restrain the deformation of the matrix phase in the vicinity of each particle, thereby increasing the strength of the material.

To confirm the validity of our experimental results, we compare the experimental results with some models. The experimental Young' modulus of the nanocomposites to Young's modulus of the pure PDMS is shown in Figure 3b, along with the results obtained from the models. The measured mechanical properties are compared with Young's moduli of the composites that were estimated from the Guth Model (Equation 3) and Halpin–Tsai model (Equation 6 and 7). Figure 3b also compares the elastic shear lag moduli (Equations 4 and 5) obtained for the nanocomposites. The results show that the experimental-determined Young's moduli are slightly larger than the predicted values, for all the reinforcement volume percentages as shown in Figure 3b.

Tensile strength was also modeled using the model by Taya and Arsenault.[42,48] The results are presented in Figure 3c. The results obtained from the model and the experiments are generally in good agreement with each other.

The good agreement between the experimental measurements and the predictions obtained for magnetite weight percentages of 1%, 5%, and 10% are associated with relatively homogeneous particle distributions. Conversely, the larger differences between the experimental data and the predictions obtained for composites with a fraction of magnetite are attributed to the effects of local stress concentration on local failure. In any case, the current results suggest that the composite mechanical properties can be engineered by controlling the reinforcement volume fractions.

TABLE 3 Weight fraction versus volume fraction

Weight fraction	Volume fraction
0.01	0.001878
0.05	0.009709
0.10	0.020279

4.4.3 | Fracture toughness

The fracture toughness values of the composites were calculated at the peak loads using Equations (9) and (10). The fracture toughness values obtained for each specimen are summarized in Table 2 and Figure 4a. The fracture toughness values of the reinforced composites were considerably greater than those of the unreinforced matrix. They increase with increasing weight percentage. The results show that, with the addition of 1 wt.% of MNPs, the fracture toughness value is within the uncertainty/error range of the fracture toughness value of pure PDMS, indicating minimal toughening is induced. Also, the fracture toughness values obtained for the composites were reinforced with 1, 5, and 10 wt.% of magnetite nanoparticles were much greater than those obtained for unreinforced PDMS.

4.4.4 | Toughening mechanisms

To further understand the fracture of the composites along with associated toughening mechanisms of the fractured composite, resistance curves were obtained for the unreinforced and nanoparticle reinforced composites (Figure 4b). The initiation toughness of values of the composites reinforced with 1%, 5%, and 10 wt.% of magnetite were $0.009\,\mathrm{MPa}\sqrt{m}$, $0.029\,\mathrm{MPa}\sqrt{m}$, and $0.018\,\mathrm{MPa}\sqrt{m}$, respectively.

Figure 5a–d present the SEM images of the notch tips of PDMS and nanoparticle reinforced composite samples that were used for the fracture test. The plain

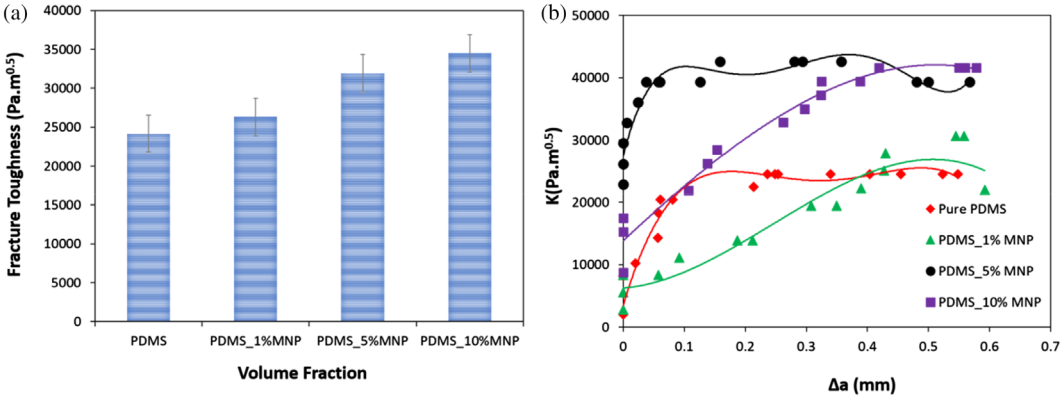


FIGURE 4 Plots of (a) fracture toughness and (b) R-curve distributions [Color figure can be viewed at wileyonlinelibrary.com]

10974628, 2022, 30, Downloaded from https://onlinelibrary.wiley.com/doi/10.1002/app.52667 by Egyptian National Sci. Network (Enstinet), Wiley Online Library on [06/11/2022]. See the Terms and Conditions (https://onlinelibrary.wiley.com/terms-and-conditions) on Wiley Online Library for rules of use; OA articles are governed by the applicable Creative Commons License

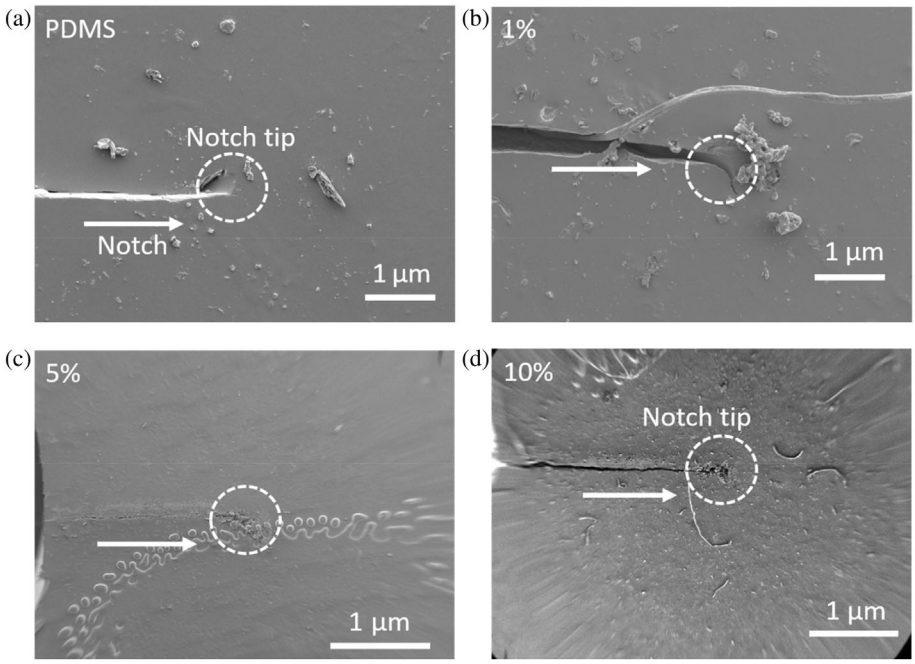


FIGURE 5 SEM images of the notch. (a) Pure PDMS, (b) PDMS + 1% MNPs, (c) PDMS + 5% MNPs, and (d) PDMS + 10% MNPs

unreinforced PDMS had a very sharp notch tip, with no evidence of nanoparticles, while the notch tips of the specimens reinforced with magnetite nanoparticles (1%, 5%, and 10 wt.%) showed evidence of the nanoparticle distributions.

The crack/microstructure profiles (side profiles) and the features on the fracture surfaces of the SENT specimens were used to determine the underlying toughening mechanisms (Figures 6 and 7). There was clear evidence of initial deflection around the nanoparticle clusters and ligament bridging by uncracked nanocomposites. Hence, the current results suggest that crack deflection and crack bridging play a role in the toughening of nanocomposites (Figures 6 and 7).

In the plain PDMS side profile, initial deflection and ligament bridging of crack followed by brittle fracture were observed. While in the fracture surface, the initial fracture surface reveals "cleavage-like river lines" in Figure 7a. This is followed by striation-like features with relatively uniform spacings. The failure mechanisms are shown clearly by comparing the two sides of the fracture surfaces (Figure S3).

In the case of the nanocomposites, the side profile of the PDMS-1%MNP specimen (Figure 6b) reveals initial crack deflection, also but limited evidence of crack tilting around nanoparticle clusters, prior to the extension of the crack beyond the initial deflected segment. The failure mechanisms observed on the fractured surfaces (Figures 7b and S4) are similar to those observed in plain PDMS, but with some interactions between crack and nanoparticle clusters. There are also some observations of striations and microvoids on the fracture surfaces.

Crack interactions with micro-pores (due to entrapped bubbles and ligament bridging) were observed in PDMS-5%

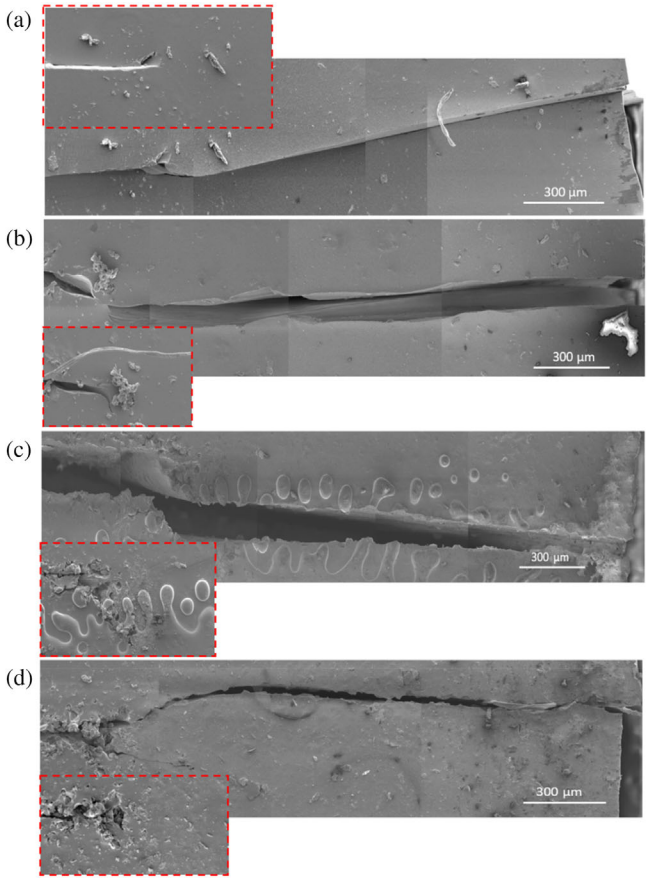


FIGURE 6 SEM images of the crack growth profiles of the composite for (a) pure PDMS, (b) PDMS + 1% MNPs, (c) PDMS + 5% MNPs, and (d) PDMS + 10% MNPs. The insets are the tips of the notch [Color figure can be viewed at wileyonlinelibrary.com]

10974628, 2022, 30, Downloaded from https://onlinelibrary.wiley.com/doi/10.1002/app.52667 by Egyptian National Sci. Network (Enstinet), Wiley Online Library on [06/11/2022]. See the Terms and Conditions (https://onlinelibrary.wiley.com/terms-and-conditions) on Wiley Online Library for rules of use; OA articles are governed by the applicable Creative Commons License

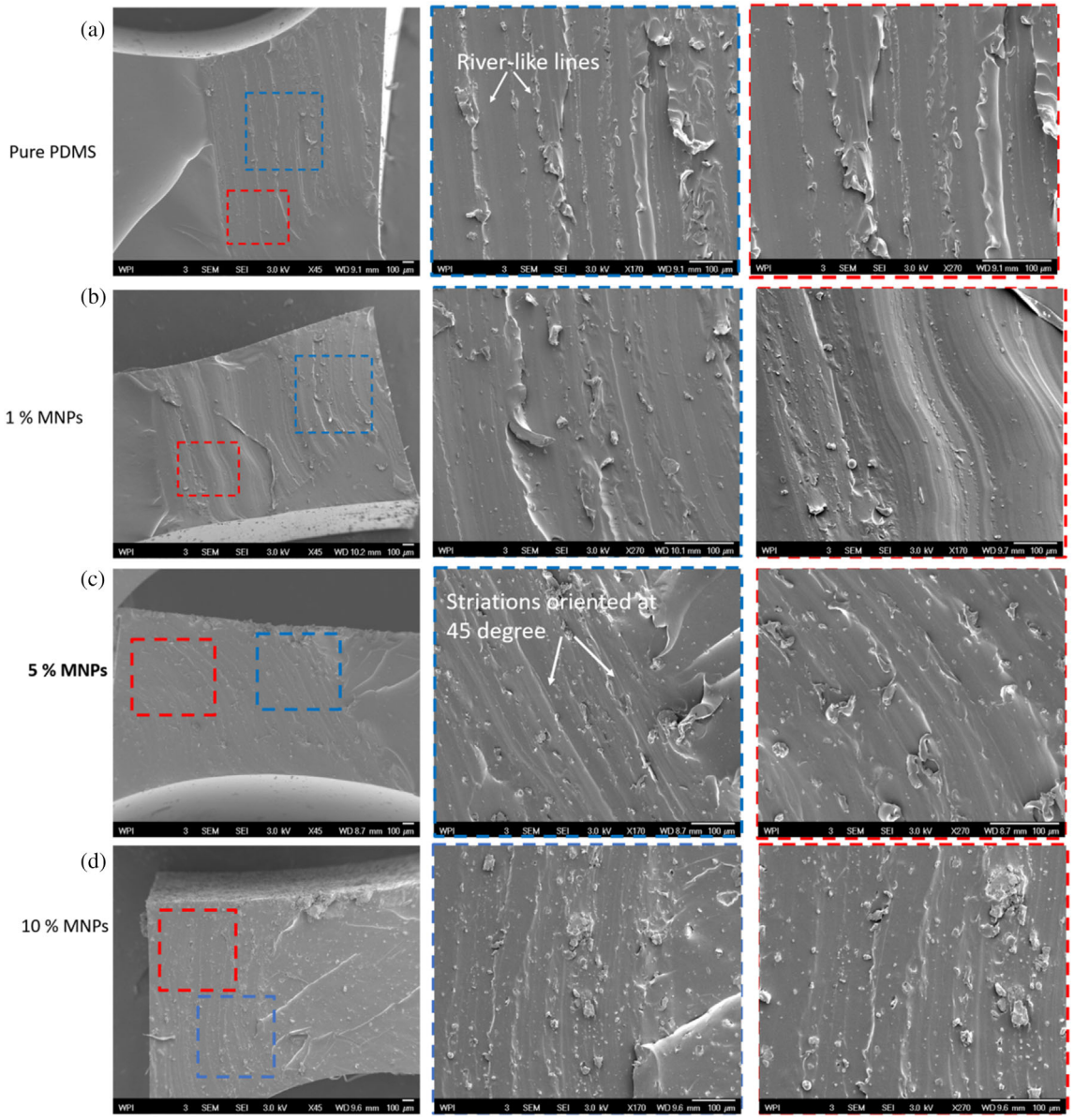


FIGURE 7 SEM images of the fracture surfaces of (a) pure PDMS, (b) PDMS + 1% MNPs, (c) PDMS + 5% MNPs, and (d) PDMS + 10% MNPs [Color figure can be viewed at wileyonlinelibrary.com]

MNPs (Figure 6c) along with ligament wedging. There is evidence of striations oriented at about 45 degrees on the fracture surfaces (Figures 7c and S5) of the 5% MNPs samples. The rough fracture surface was observed presumably due to more frequent crack/nanoparticle cluster interactions. Interactions between striations, internal porosity, and nanoparticle clusters were also observed.

Finally, deflected and wedged crack segments with evidence of bridging ligaments and fractured ligaments were observed along the crack path of PDMS − 10% MNP (Figure 6d). The fractured surfaces (Figures 7d and S6) showed evidence of crack interactions with nanoparticle clusters and micro-pores as seen in 5%. There is also evidence of secondary microcracks oriented along striations that were inclined at about 45 degrees to the direction of crack growth was observed.

To further elucidate the shielding mechanisms, the toughening due to crack deflection and small-scale bridging (SSB)[52] were compared with experimental results. Figure 8a–c presents comparisons between the experimental results and those predicted by the models. The predictions obtained from the crack deflection models were generally in good agreement with the experimental measurements of fracture toughness. Figure S7 also presents a comparison of the results obtained from crack deflection model with those from experiments. These are generally in good agreement with each other, indicating that crack deflection plays a significant role in enhancing fracture toughness.

10974628, 2022, 30, Downloaded from https://onlinelibrary.wiley.com/doi/10.1002/app.52667 by Egyptian National Sci. Network (Enstinet), Wiley Online Library on [06/11/2022]. See the Terms and Conditions (https://onlinelibrary.wiley.com/terms-and-conditions) on Wiley Online Library for rules of use; OA articles are governed by the applicable Creative Commons License

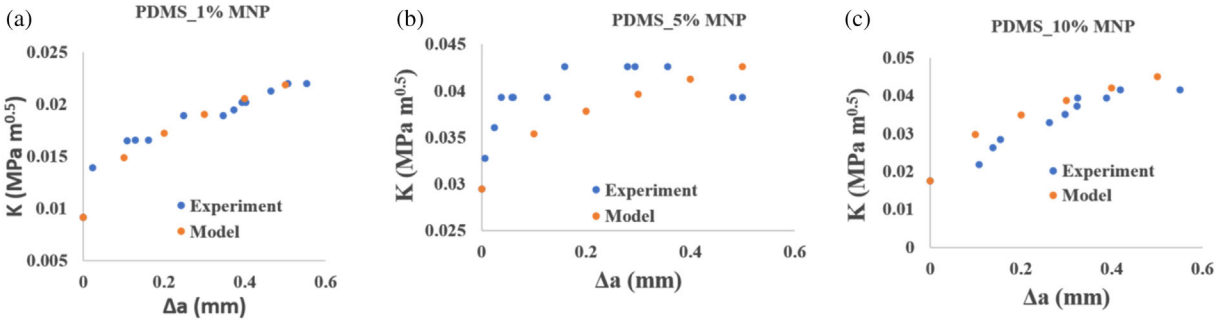


FIGURE 8 Toughening mechanism due to small scale bridging for (a) 1%, (b) 5%, and (c) 10% volume fractions [Color figure can be viewed at wileyonlinelibrary.com]

4.5 | Comparisons with breast tissue mechanical properties

Finally, in this section, it is of interest to compare the mechanical properties of the PDMS nanocomposites implants with those of breast tissue (mammary glands or adipose tissue). However, very limited quantitative information is available on the biomechanical properties of soft tissues, which do not have an active mechanical function such as the breast,[67] although several researchers have quantified the mechanical properties of the breast constituents using the Young's moduli the type of tissue which are usually measured under compression.

Also, comprehensive knowledge of the mechanical properties of glandular and adipose tissue is not yet available in the literature. According to Krouskop et al.,[68] the Young's moduli of the breast tissues are highly dependent on the level of tissue preload compression used in the measurements, and the moduli increased significantly with additional compression. Studies have also shown that tumors are much stiffer than normal breast tissues, that tumor tissue is not only much stiffer than adipose and normal glandular tissue but displays a higher nonlinear increase in Young's moduli.[68,69] Several authors model the behavior of the tissue using a single elastic or shear modulus[67,69] assuming that soft biological tissue is predominately composed of water an incompressible fluid, it is considered incompressible.[70]

According to the review by Ramião et al.[71] the Young's moduli of normal glandular tissues range from 0.73 to 271 kPa, while those of tumor tissue ranges from 10 to 13,665 kPa for ex-vivo breast tissue, these mechanical properties range reported by the different authors shows a significant variability which makes it difficult to use statistical data to model the individual properties of the breast showing that the stiffness of breast tissue is highly dependent on the tissue preloaded compression level.

Cox and Erler[43] have reported the Young's modulus of breast tissue to be approximately between 800 and 1200 kPa, while Gefen and Dilmony have reported the Young modulus of breast tissue to be approx. 7.5–66 kPa (glandular tissue), 0.25 kPa (adipose tissue), and 200–3000 kPa (skin tissue), while the UTS has for the skin is approx. 20 MPa.[72]

These results show that there is no clear recorded Young's moduli of the breast tissue in the literature.[71] Our experimental data give Young's moduli of 1.83 to 2.5 MPa, which also agrees with prior reports of the breast skin modulus and that of tumor tissues,[14] although slightly different from that of Cox and Erler.[43] Thus, the results obtained from the current literature indicate a wide variation in the Young's moduli of the composite devices and those of normal tissue. Surprisingly, there are no data in the literature regarding fracture toughness/resistance-curve behavior of the breast tissues.

Finally, it is important to note that the similarities in the Young's moduli of the magnetite nanocomposites and those of breast tissue suggest that minimal stress-shielding will occur in the surrounding breast tissues (around the implant). This should lead to improved long term integration between the device and the surrounding breast tissue. Further work is clearly needed to explore the long term integration of the PDMS/magnetite nanocomposites with animal and human tissues. These are clearly opportunities for future animal and human trials.

5 | SUMMARY AND CONCLUDING REMARKS

In this study, we have successfully used a combination of experiments and theoretical models to study the mechanical and thermal properties of magnetite nanoparticle-reinforced PDMS composites for potential applications in hyperthermia and/or photoablation for cancer treatment. The nanocomposites were fabricated by mixing magnetite nanoparticles with PDMS to form magnetite nanoparticle-reinforced PDMS composites with different weight fractions.

10974628, 2022, 30, Downloaded from https://onlinelibrary.wiley.com/doi/10.1002/app.52667 by Egyptian National Sci. Network (Enstinet), Wiley Online Library on [06/11/2022]. See the Terms and Conditions (https://onlinelibrary.wiley.com/terms-and-conditions) on Wiley Online Library for rules of use; OA articles are governed by the applicable Creative Commons License

1. The mechanical properties (tensile strength, the Young's modulus, and the fracture toughness) have been effectively improved by reinforcement with magnetite nanoparticles,. After introducing the nanoparticles, the Young's modulus of the nanocomposites increased from 1.87 ± 0.01 to 2.54 ± 0.05 MPa. This increase in the Young's modulus is well predicted by the GuthGold, Halpia-Tsai, and shear lag models
2. The similarities in the Young's moduli of the PDMS composites and those of breast tissue suggest that the nanocomposites examined in this study can be used as implants in breast tissues, without inducing significant stress shielding phenomena in the surrounding breast tissues.
3. The fracture toughness also increases from 0.0241 ± 0.05 to 0.0345 ± 0.01 MPa.m,$^{1/2}$ for paticle weight percentages between 0 and 10. The fracture toughness is enhanced to 0.0345 MPa.m$^{1/2}$ for the polymer nanocomposites (about 50% increase) with a 10 wt.% of magnetite nanoparticles. (Figure 3b). These are associated with evidence of toughening by crack deflection/crack tilting around nanoparticle clusters, and crack-tip shielding by bridging ligaments (Figure 6a–d).
4. The fracture toughness and resistance-curve behavior of the nanocomposites also depend on magnetite nanoparticle reinforcement. The measured fracture toughness/resistance-curve behavior are also consistent with the predicted fracture toughness/resistance-curve behavior. The toughening is associated with crack-tip shielding by crack deflection and crack bridging.

AUTHOR CONTRIBUTIONS

Chinyerem E. Onyekanne: Conceptualization (supporting); data curation (lead); formal analysis (lead); investigation (lead); methodology (lead); writing – original draft (lead). **Oluwaseun K. Oyewole:** Conceptualization (equal); formal analysis (equal); investigation (equal); supervision (equal); writing – review and editing (equal). **Ali A. Salifu:** Data curation (equal); formal analysis (equal); supervision (equal); validation (lead); visualization (lead); writing – review and editing (equal). **John D. Obayemi:** Formal analysis (equal); investigation (equal); supervision (equal); visualization (supporting); writing – review and editing (equal). **Vitalis C. Anye:** Investigation (supporting); methodology (lead); resources (supporting); writing – original draft (supporting); writing – review and editing (supporting). **Chukwudalu C. Nwazojie:** Data curation (supporting); formal analysis (supporting); writing – review and editing (supporting). **Killian C. Onwudiwe:** Formal analysis (supporting); writing – review and editing (supporting). **Josephine C. Oparah:** Data curation (supporting); formal analysis (supporting); writing – review and editing (supporting). **Toyin Aina:** Writing – review and editing (supporting). **Chukwudi C. Ezeala:** Writing – review and editing (supporting). **Theresa C. Ezenwafor:** Writing – review and editing (supporting). **Olushola S. Odusanya:** Supervision (equal); writing – review and editing (equal). **Winston O. Soboyejo:** Conceptualization (lead); formal analysis (supporting); investigation (lead); methodology (supporting); supervision (lead); validation (supporting); writing – review and editing (supporting).

ACKNOWLEDGMENTS

The authors will like to thank the Pan African Material Research Institute (PAMI) with funding from the World Bank African Centers of Excellence (ACE) (Grant No. P126974) at the African University of Science and Technology, Abuja, Nigeria, and the Global Fellowship at the Worcester Polytechnic Institute (WPI), MA, USA for their financial support.

DATA AVAILABILITY STATEMENT

The data that support the findings of this study are available on request from the corresponding author. The data are not publicly available due to privacy or ethical restrictions.

ORCID

Winston O. Soboyejo https://orcid.org/0000-0002-0209-1079

REFERENCES

[1] Bourgeat-Lami E, Duguet E. *Functional Coatings: By Polymer Microencapsulation*, Wiley, Belgium **2006**. https://doi.org/10.1002/3527608478.ch4
[2] M. M. S. D. S. De Bustamante, R. P. C. Neto, I. C. S. Santos, E. O. Da Silva, M. I. B. Tavares, *Mater. Res.* **2012**, *15*, 825.
[3] C. Wu, *J. Appl. Polym. Sci.* **2003**, *89*, 2888.
[4] T. Hanemann, D. V. Szabó, *Materials* **2010**, *3*, 3468.
[5] E. Malikmammadov, T. E. Tanir, A. Kiziltay, V. Hasirci, *PCL and PCL-Based Materials in Biomedical Applications*, Vol. 5063, Taylor & Francis, London **2017**.
[6] A. Victor, J. F. Ribeiro, F. Araújo, *J. Mech. Eng. Biomech.* **2019**, *4*, 1.
[7] W. Xu, N. Chahine, T. Sulchek, *Langmuir* **2011**, *27*, 8470.
[8] J. S. Park, R. Cabosky, Z. Ye, I. Kim, (Isaac)., *Opt. Mater.* **2018**, *85*, 153.
[9] A. Zahid, B. Dai, R. Hong, D. Zhang, *Mater Res Express.* **2017**, *4*, 105301. https://doi.org/10.1088/2053-1591/aa8645
[10] I. Teixeira, I. Castro, V. Carvalho, C. Rodrigues, A. Souza, R. Lima, S. Teixeira, J. Ribeiro, *AIMS Mater Sci.* **2021**, *8*, 952.
[11] K. Kan-Dapaah, N. Rahbar, A. Tahlil, D. Crosson, N. Yao, W. Soboyejo, *J. Mech. Behav. Biomed. Mater.* **2015**, *49*, 118.
[12] W. Gao, X. Wang, W. Xu, *Polym. Compos.* **2019**, *40*, 337.
[13] I. Miranda, A. Souza, P. Sousa, J. Ribeiro, E. M. S. Castanheira, R. Lima, G. Minas, *J Funct Biomater.* **2022**, *13*, 2.
[14] A. H. M. Yusoff, M. N. Salimi, in *Superparamagnetic Nanoparticles for Drug Delivery. Applications of Nanocomposite*

10974628, 2022, 30, Downloaded from https://onlinelibrary.wiley.com/doi/10.1002/app.52667 by Egyptian National Sci. Network (Enstinet), Wiley Online Library on [06/11/2022]. See the Terms and Conditions (https://onlinelibrary.wiley.com/terms-and-conditions) on Wiley Online Library for rules of use; OA articles are governed by the applicable Creative Commons License

Materials in Drug Delivery, 1st ed. (Eds: A. A. M. Inamuddin, A. Mohammad), Woodhead Publishing, Cambridge, MA **2018**. https://doi.org/10.1016/B978-0-12-813741-3.00037-6
[15] K. M. Krishnan, *IEEE Trans. Magn.* **2010**, *46*, 2523.
[16] H. Markides, M. Rotherham, A. J. El Haj, *J. Nanomater.* **2012**, *2012*, 13.
[17] J. Gavard, S. Hanini, *Int. J. Nanomed.* **2011**, *6*, 787.
[18] M. Bustamante-Torres, D. Romero-Fierro, J. Estrella-Nuñez, B. Arcentales-Vera, E. Chichande-Proaño, E. Bucio, *Polymers* **2022**, *14*, 752.
[19] R. A. R. Zhang, M., *Physiol. Behav.* **2017**, *176*, 139.
[20] M. Kawashita, K. Kawamura, Z. Li, *Acta Biomater.* **2010**, *6*, 3187.
[21] K. Kan-Dapaah, N. Rahbar, W. Soboyejo, *Appl. Phys.* **2014**, *116*, 233505.
[22] C. L. Wu, H. C. Lin, J. S. Hsu, M. C. Yip, W. Fang, *Thin Solid Films* **2009**, *517*, 4895.
[23] A. Goyal, A. Kumar, P. K. Patra, S. Mahendra, S. Tabatabaei, P. J. J. Alvarez, G. John, P. M. Ajayan, *Macromol. Rapid Commun.* **2009**, *30*, 1116.
[24] J. Liu, G. Zong, L. He, Y. Zhang, C. Liu, L. Wang, *Micromachines* **2015**, *6*, 855.
[25] Y. Konku-Asase, A. Yaya, K. Kan-Dapaah, *Adv. Mater Sci Eng.* **2020**, *1*.
[26] A. Shafaamri, C. H. Cheng, I. A. Wonnie Ma, S. B. Baig, R. Kasi, R. Subramaniam, V. Balakrishnan, *Front Mater.* **2020**, *6*, 1.
[27] J. Beik, Z. Abed, F. S. Ghoreishi, S. Hosseini-Nami, S. Mehrzadi, A. Shakeri-Zadeh, S. K. Kamrava, *J. Controlled Release* **2016**, *235*, 205.
[28] J. Estelrich, B. M. Antònia, *Molecules* **2018**, *23*, 1567.
[29] R. A. Green, N. H. Lovell, G. G. Wallace, L. A. Poole-Warren, *Biomaterials* **2008**, *29*, 3393.
[30] B. D. Ratner, S. J. Bryant, *Annu. Rev. Biomed. Eng.* **2004**, *6*, 41.
[31] P. M. Klinge, M. A. Vafa, T. Brinker, A. Brandis, G. F. Walter, T. Stieglitz, M. Samii, K. Wewetzer, *Biomaterials* **2001**, *22*, 2333.
[32] W. Wu, Z. Wu, T. Yu, C. Jiang, W. S. Kim, *Sci Technol Adv. Mater* **2015**, *16*, 023501.
[33] A. H. Lu, E. L. Salabas, F. Schüth, *Angew Chemie - Int Ed.* **2007**, *46*, 1222.
[34] Y. K. Konku-Asase, K. Kan-Dapaah, *Materials* **2021**, *14*, 1.
[35] M. Liu, J. Sun, Q. Chen, *Sens. Actuat. A Phys.* **2009**, *151*, 42.
[36] I. D. Johnston, D. K. McCluskey, C. K. L. Tan, M. C. Tracey, *J Micromech. Microeng.* **2014**, *24*, 035017.
[37] M. A. Campeau, A. Lortie, P. Tremblay, M. O. Béliveau, D. Dubé, È. Langelier, L. Rouleau, *J. Geophys. Res. Planets* **2017**, *16*, 1.
[38] N. K. Kwon, H. Kim, I. K. Han, T. J. Shin, H. W. Lee, J. Park, S. Y. Kim, *ACS Macro Lett.* **2018**, *7*, 962.
[39] A. Kumar, K. Sharma, A. R. Dixit, *Carbon Lett.* **2021**, *31*, 149.
[40] D. Arencón, J. I. Velasco, *Materials* **2009**, *2*, 2046.
[41] E. D. Bliznakov, C. C. White, M. T. Shaw, *J. Appl. Polym. Sci.* **2000**, *77*, 3220.
[42] W. O. Soboyejo, R. J. Lederich, S. M. L. Sastry, *Acta Metall. Mater.* **1994**, *42*, 2579.
[43] T. R. Cox, J. T. Erler, *DMM Dis Model Mech.* **2011**, *4*, 165.
[44] V. C. Nardone, K. M. Prewo, *Scr Metall.* **1986**, *20*, 43.
[45] T. H. Hsieh, A. J. Kinloch, K. Masania, A. C. Taylor, S. Sprenger, *Polymer* **2010**, *51*, 6284.
[46] B. B. Johnsen, A. J. Kinloch, R. D. Mohammed, A. C. Taylor, S. Sprenger, *Polymer* **2007**, *48*, 530.
[47] J. C. H. Affdl, J. L. Kardos, *Polym. Eng. Sci.* **1976**, *16*, 344.
[48] R. J. Arsenault, M. Taya, *Acta Metall.* **1987**, *35*, 651.
[49] X. K. Zhu, *Fatigue Fract. Eng. Mater. Struct.* **2016**, *39*, 120.
[50] Tada HPCP and GRI, *The Stress Analysis of Cracks Handbook*, 3rd ed., Springer, New York **2000**.
[51] E. B. Ojo, K. O. Bello, O. F. Ngasoh, T. T. Stanislas, K. Mustapha, H. Savastano Jr., W. Soboyejo, *Constr. Build. Mater.* **2020**, *247*, 118588.
[52] B. Budiansky, J. C. Amazigo, A. G. Evans, *J. Mech. Phys. Solids* **1988**, *36*, 167.
[53] Q. Qin, J. Ye, *Toughening Mechanisms in Composite Materials*, Woodhead Publishing, Sawston, UK **2015**.
[54] M. Bengisu, O. T. Inal, *J. Mater. Sci.* **1994**, *29*, 5475.
[55] A. Groza, A. Surmeian, *J. Nanomater.* **2015**, *2015*, 1.
[56] L. Nalbandian, A. Patrikidou, E. Hatzidaki, C. N. Papandreou, *Current Nanosci.* **2015**, *12*, 455.
[57] E. Bertolucci, A. M. R. Galletti, C. Antonetti, M. Marracci, B. Tellini, F. Piccinelli, C. Visone, Proceedings of the 2015 IEEE International Instrumentation and Measurement Technology Conference (I2MTC) 2015, 1492–1496. https://doi.org/10.1109/I2MTC.2015.7151498
[58] L. M. Al-Harbi, M. S. A. Darwish, M. M. Khowdiary, I. Stibor, *Polymers* **2018**, *10*, 507.
[59] N. Grassie, I. G. Macfarlane, *Eur. Polym. J.* **1978**, *14*, 875.
[60] D. E. Kherroub, T. Boulaouche, *Res. Chem. Intermed.* **2020**, *46*, 5199.
[61] S. Dutz, R. Hergt, *Int J Hyperth.* **2013**, *29*, 790.
[62] A. Choudhury, A. K. Bhowmick, C. Ong, M. Soddemann, *J. Nanosci. Nanotechnol.* **2010**, *10*, 5056.
[63] J. Junges, A. J. Zattera, L. S. Lima, L. B. Gonella, J. Junges, A. J. Zattera. Conference: Polymer Processing Society 29th Annual Meeting At: Nuremberg (Germany) 2013, 1–5. https://doi.org/10.13140/RG.2.1.4396.0168
[64] R. Ariati, F. Sales, A. Souza, R. A. Lima, J. Ribeiro, *Polymers* **2021**, *13*, 4258.
[65] T. Saotome, K. Kokubo, S. Shirakawa, T. Oshima, H. T. Hahn, *J. Compos. Mater.* **2011**, *45*, 2595.
[66] S. Y. Fu, X. Q. Feng, B. Lauke, Y. W. Mai, *Compos. B Eng.* **2008**, *39*, 933.
[67] A. Samani, J. Zubovits, D. Plewes, *Phys. Med. Biol.* **2007**, *52*, 1565.
[68] T. A. Krouskop, T. M. Wheeler, F. Kallel, B. S. Garra, T. Hall, *Ultrason Imaging.* **1998**, *20*, 260.
[69] P. S. Wellman, R. D. Howe, E. Dalton, K. A. Kern, Breast Tissue Stiffness in Compression is Correlated to Histological Diagnosis. Technical Report Harvard BioRobotics Lab 1999, 1–15.
[70] Y. C. Fung, *Appl Mech* **1994**, *61*, 568.
[71] N. G. Ramião, P. S. Martins, R. Rynkevic, A. A. Fernandes, M. Barroso, D. C. Santos, *Biomech Model Mechanobiol.* **2016**, *15*, 1307.
[72] A. Gefen, B. Dilmoney, *Technol. Health Care* **2007**, *15*, 259.

SUPPORTING INFORMATION

Additional supporting information may be found in the online version of the article at the publisher's website.

How to cite this article: C. E. Onyekanne, O. K. Oyewole, A. A. Salifu, J. D. Obayemi, V. C. Anye, C. C. Nwazojie, K. C. Onwudiwe, J. C. Oparah, T. Aina, C. C. Ezeala, T. C. Ezenwafor, O. S. Odusanya, W. O. Soboyejo, *J. Appl. Polym. Sci.* **2022**, *139*(30), e52667. https://doi.org/10.1002/app.52667

10974628, 2022, 30, Downloaded from https://onlinelibrary.wiley.com/doi/10.1002/app.52667 by Egyptian National Sci. Network (Enstinet), Wiley Online Library on [06/11/2022]. See the Terms and Conditions (https://onlinelibrary.wiley.com/terms-and-conditions) on Wiley Online Library for rules of use; OA articles are governed by the applicable Creative Commons License